Integrated in-situ imaging and diffraction flow cell technology (NX-DRT) for advanced corrosion studies

Vicky Ullas Mirashi [a,b,c], Winfried Kockelmann [c], Nikil Kapur [a,b], Adriana Matamoros-Veloza [a,d,*]

[a] Faculty of Engineering and Physical Sciences, University of Leeds, Leeds LS2 9JT, UK
[b] School of Mechanical Engineering, University of Leeds, Leeds LS2 9JT, UK
[c] STFC-Rutherford Appleton Laboratory, ISIS Facility, Harwell OX11 0QX, UK
[d] School of Chemistry, University of Leeds, Leeds LS2 9JT, UK

ARTICLE INFO

ABSTRACT

Dynamic imaging and mechanistical investigations are crucial in the development of new materials, in understanding degradation and offer significant opportunity across diverse areas of materials research. Here we demonstrate the integration of a sample corrosion environment with imaging through low energy neutrons and synchrotron X-rays, and demonstrate this using steel, which is commonly used in the oil and gas industries. The novel flow cell technology, incorporating three-electrodes to link corrosion with imaging (2D and 3D with neutrons and X-rays) is unique and operates in-situ overcoming limitations around manipulating the environment around the sample. The compact flow cell enabled imaging of thin films of a few microns thickness. The combination of imaging and diffraction data are useful to characterize the degradation mechanism qualitatively and quantitatively over time with 3D tomography used to provide visual and volumetric information on film growth, porosity and pitting position. This work demonstrates the unprecedented capability of the in-situ flow cell to conduct degradation studies and elucidate mechanisms in ways never before possible.

1. Introduction

Corrosion is a natural and inevitable process that leads to the gradual deterioration of materials reducing their strength, appearance, functionality and posing a significant challenge to industries (e.g., oil and gas, CO_2 transportation, food processing and manufacturing), economy and society due to safety concerns and environmental issues [1–6]. Low carbon steel is the preferred material for many of the industrial applications due to its low cost and other good mechanical properties that make this material less prone to becoming brittle, ductile, having good weldability and ability to withstand high internal pressures. Pipelines made of low carbon steel (from 0.1 % to 0.16 % carbon) are the primary mode of transport of oil and gas, an industry that currently provides more than half of the energy consumed worldwide [7]. High-strength low-alloy (HLSA) American Petroleum Institute (API) 5 L X grades are the preferred materials due to their superior mechanical properties but they readily corrode in fluid at harsh environment conditions (e.g., high temperature, high pressure) increasing their risk of failure [2,8,9]. Fig. 1 exemplifies the types of sweet corrosion, caused by the interaction of the material with a CO_2 saturated fluid containing sodium chloride causing general corrosion and localized corrosion with evolution of pits [10–12].

Corrosion studies frequently rely on scanning electron microscopy (SEM) to observe the surface of the metal substrate regarding type of corrosion and morphology but this technique neither provides information underneath the film nor the damaging process of the substrate as corrosion evolves. Although it provides microstructural information to some extent, it is unable to correlate the damage of the substrate with chemical changes on the surface [13–19]. Currently, the degradation status underneath the film can only be observed after removal of the corrosion film or by preparing a cross section of the sample. Therefore, it is imperative to have a non-destructive technique that provides information about (i) steel degradation - microstructural changes and features on steel surface due to corrosion such as pits; (ii) corrosion film - morphology of corrosion products, film formation and porosity; (iii) phase formation and transformation during the corrosion process. The best option to achieve this would be a technique capable of combining 3D imaging with diffraction – currently non-existent.

Neutron and X-ray radiation offer contrasting and complementary

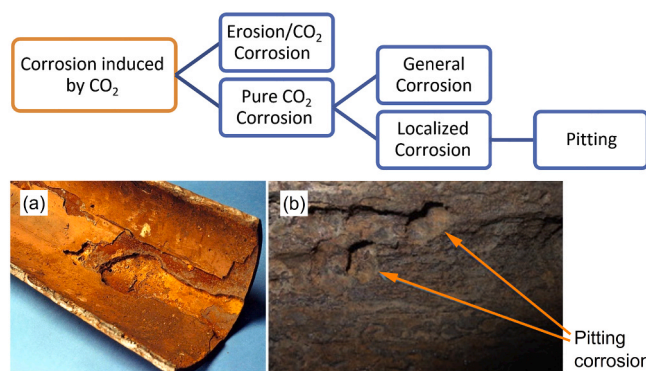* Corresponding author at: Faculty of Engineering and Physical Sciences, University of Leeds, Leeds LS2 9JT, UK.
E-mail address: A.MatamorosVeloza@leeds.ac.uk (A. Matamoros-Veloza).

Fig. 1. Internal corrosion occurring in oil and gas pipelines. (a) general corrosion, (b) pitting corrosion caused by CO_2 corrosion. Reproduced from [11, 20,21].

characteristics of interest for the study of materials. Both types of radiation have the capability to pass through materials but analysing steel with X-rays is challenging due to the density of this material [22]. Neutrons have higher penetration depth in materials, compared to electrons and X-rays, whilst X-rays offer higher spatial resolution compared to neutrons. Neutron imaging has shown to be the most effective way for examining dense (e.g., iron, copper, tungsten) and bulk metallic samples with volumes up to 100 cm^3. Neutrons also show high sensitivity to light elements (e.g., hydrogen, lithium, boron) making this radiation of great interest for material studies. Neutron imaging allows us to conduct attenuation-based and isotropic sensitivity studies, and to achieve magnetic imaging of internal magnetic fields. On the other hand, analysis of steel using X-rays requires a reduction on the cross section of the sample to overcome low penetration depths but allows high spatial resolution of the order of a few microns beneficial to resolve features at microscopic level enabling a complementary comparison of the data obtained from neutrons [23].

Advances in combined imaging and diffraction techniques capable of collecting in-situ information would be a superior approach to study corrosion and degradation of materials that requires the use of a flow cell for analysis [24]. Few flow cells have been used in the past to investigate corrosion processes; for example, a flow-accelerated cell has been used to study corrosion in CO_2 environments [25,26], and a once-through flow cell has been employed to investigate microbiological influenced corrosion [27,28]. Flow cells has been utilized for synchrotron radiation grazing incidence X-ray diffraction analysis [29], for aqueous corrosion at elevated temperatures or pressures [24], and to study flow dependent corrosion [30]. Electrochemical cells have been used for in-situ studies of degradation using small-angle X-ray scattering [31], imaging using atomic force microscopy [32], and 2D imaging using microscopy and spectroscopy [33]. However, to our knowledge a flow cell that performs for 2D and 3D imaging combined with diffraction and that complies with instrument and technique requirements whilst also satisfy application demands is lacking.

This work presents the development of an in-situ imaging and diffraction technique for corrosion studies using neutron and X-ray imaging at the Imaging and Material Science & Engineering (IMAT, ISIS, UK) [34] and at the Dual Imaging and Diffraction beamline (DIAD, Diamond Light Source, UK) [35]. Advanced, in-situ and high resolution techniques are essential to understand the corrosion mechanism at the micron scale, beyond the capabilities of standard laboratory methods. Transfer of the development technology could be possible if laboratory instruments further develop to improve resolution or if the research questions fall within the spatial resolution range. For instance, 3D imaging at NXCT facility (Manchester, UK) achieves 2–5 µm voxel size [36] for steel in contrast to 0.5 µm voxel size at DIAD beamline with higher flux. Considerations and design of the flow cell for analysis using both neutron and X-rays radiation applicable to 2D (radiography) and 3D

(tomography) imaging as well as diffraction are presented. Performance of the flow cell is effectively demonstrated through corrosion applications. Overall, our contribution with this work to the materials field lies on the provision of an in-situ technique that allows for imaging and diffraction analysis as a reaction on the material proceeds and it is exemplified on a corrosion reaction for the subsequent evaluation of pit formation and determination of porosity and thickness of the metal substrate. Such a technique brings new understanding to the corrosion processes and could underpin new material developments.
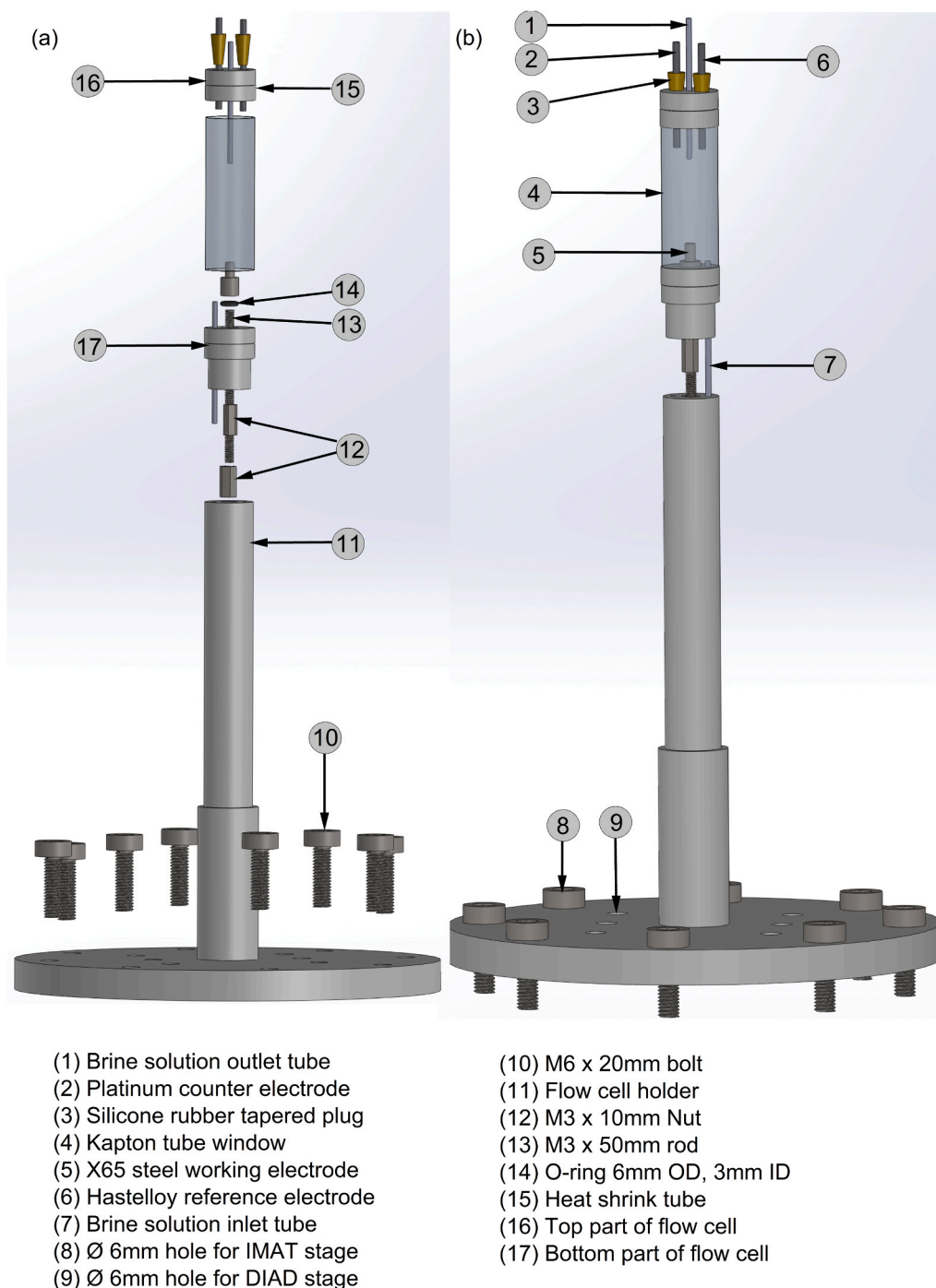
2. NX-DRT Flow cell design

The Neutron, X-ray Diffraction, Radiography and Tomography (NX-DRT) flow cell is a three-electrode flow cell, designed for in-situ imaging and diffraction that allows the simultaneous acquisition of electrochemical data to investigate corrosion and steel degradation. Various aspects were considered for the development of the flow cell to include requirements of neutron and X-rays beamlines and techniques, the technical application, and practicalities of the methods. The development involved three work fronts (1) flow cell design and development, (2) corrosion reactions, and (3) imaging techniques. Off-line tests and measurements were initially conducted on steel corroded samples to first highlight the requirements of the beamlines and techniques. The initial design was subjected to various iterations until the final design of the flow cell was achieved.

2.1. Flow cell design requirements

The flow cell designed for imaging and diffraction experiments must be cylindrical to enable full 360-degree rotational scanning and maintain geometric symmetry. It must be airtight to prevent external contamination, accommodating inlet and outlet tubing, as well as working, counter, and reference electrodes. To enhance imaging resolution and expedite tomography scans, the cell needs to be positioned close to the detector, with the working electrode (≤5 mm in diameter), centrally located. The electrolyte solution needs to flow bottom-up during corrosion experiments to avoid gas trapping. The flow cell window must have low scattering and high transmission for neutrons and X-rays to ensure a high signal-to-noise ratio. Additionally, the cell holder, fixed to the beamline stage, should match the cell diameter to preserve imaging resolution. Further details on the design requirements are listed in the supplementary information (SI).

2.2. Flow cell design

The flow cell was designed to comprise three main parts, (1) top part of the flow cell body, (2) bottom part of the flow cell body and (3) the window of the cell. Top and bottom parts were made of HTM140 material able to hold up to temperature of 140 °C. The flow cell window was made with a custom-made Kapton tube that resists up to 400 °C, in addition of being transparent to neutrons and X-rays. The top part, bottom part and a custom-made Kapton tube are assembled and sealed using a heat shrink jacket. The cell was designed to be a compact cylinder to accommodate all its components. The top part of the flow cell has three holes to fit the electrolyte outlet tubing, a counter and a reference electrode (Fig. 2). The inlet and outlet tubing (1.6 mm diameter) are fitted to the bottom and top part of the cell. Both counter (Platinum) and reference (Hastelloy) electrodes are secured to the cell with the help of rubber stoppers (Fig. 2). The bottom part of the cell has an inlet to accommodate the working electrode (X65 steel), and a hole to insert the tubing carrying the electrolyte. Fig. 2 shows the working electrode positioned at the centre of the cell as the centre of rotation for tomography analysis. The bottom part of the cell has a step, 16 mm to 14 mm, to provide optional space for the cell holder rod. The cell holder is a hollow rod and fixed to a 3D printed adapter plate or to a 4-jaw chuck mounted on the beamline rotating stage.

Fig. 2. (a) Exploded view of NDRT flow cell setup, (b) Schematic representation assembled flow cell setup (OD: Outer Diameter, ID: Inner Diameter).

(1) Brine solution outlet tube
(2) Platinum counter electrode
(3) Silicone rubber tapered plug
(4) Kapton tube window
(5) X65 steel working electrode
(6) Hastelloy reference electrode
(7) Brine solution inlet tube
(8) Ø 6mm hole for IMAT stage
(9) Ø 6mm hole for DIAD stage

(10) M6 x 20mm bolt
(11) Flow cell holder
(12) M3 x 10mm Nut
(13) M3 x 50mm rod
(14) O-ring 6mm OD, 3mm ID
(15) Heat shrink tube
(16) Top part of flow cell
(17) Bottom part of flow cell

2.3. Steel sample design

The X65 sample (working electrode) was designed to fit the bottom part of the flow cell with a diameter of 3 mm at the top, and 6 mm at the bottom with a threaded hole (M3x0.5 mm) of 4 mm depth. The hole allows to fasten the electrode to the threaded rod that connects to the cell holder. The sample is sealed tightly using an O-ring placed underneath the sample to avoid leakage of electrolyte, and to restrain oxygen from entering the cell. The threaded rod connected to the working electrode can be coupled to heater cartridges in case of heating requirements. Unlike neutrons, X-rays do not penetrate deep into the steel material requiring a substantially narrower cross-section, hence, the top surface of the sample was slanted at 45° for analysis with low energy X-

rays. The bottom part of the sample was kept at 6 mm in diameter to ensure a comfortable fit inside the flow cell.

2.4. Flow cell holder design

A flow cell holder was also designed and built to allow the attachment of the flow cell to the sample stage at the neutron and X-ray facilities. It was manufactured using Acrylonitrile Styrene Acrylate (ASA) thermoplastic material to offer electrical resistance. The cell holder was built considering the design requirements of both types of facilities. The holder features 6 inner M6 holes (Ø6 mm diameter) and 8 outer M6 holes angled at 45° across the circumference of the bottom plate allowing the holder to be fixed to different beamline stages. A jacket of

up to 50 mm height was added to the bottom part of the holder rod to provide stability to the holder and to diminish vibrations that affect high-resolution tomography analysis. To further enhance stability, the top part of the holder was fitted with two M3 nuts to hold the M3 threaded rod at the other end of the working electrode.

2.5. Flow cell specifications

Table 1
Flow cell specifications. ID - inner diameter, OD - outer diameter, PTFE - Polytetrafluoroethylene.

Flow cell dimensions	16 mm diameter and 70 mm height
Material	HTM140, Kapton
Operating temperature limit	140 °C limited by beamline
Flow rate	≤ 0.2 m/s for long runs over days without any leakages
Kapton tube	16 mm inner diameter, 50 mm height and 0.1 mm thickness
Sample size	3 mm top diameter and 6 mm bottom diameter with M3 x 0.5 mm threaded hole
O-ring	6 mm OD and 4 mm ID
Counter and reference electrodes	Platinum and Hastelloy wire of 1 mm diameter each
Inlet and Outlet tubing (PTFE)	1/16" OD and 0.031" ID
Taper shaped solid rubber stopper	3 mm and 7 mm diameter at two ends with 1 mm diameter hole for electrodes
Heat shrink tube	19 mm sleeve diameter with 3:1 shrink ratio

2.6. Final assembly of the NX-DRT flow cell

The final version of the NX-DRT flow cell designed in SolidWorks [37] is shown in Fig. 2. The flow cell assembly consisted in mounting the counter and reference electrodes (2) and (6) to the top part of the flow cell (16) with a tapered rubber stopper (3) to provide an air-tight seal. This was followed by introducing two pieces of tubing (1) and (7), one to the top and one to the bottom part of the cell, which serve as the inlet and outlet ports for the flow of brine solution through the flow cell. The working electrode opening was lined with an O-ring (14) of 6 mm outer diameter and 3 mm inner diameter. A steel sample (5) was inserted to the bottom part of the flow cell (17), just above the O-ring and tightened with an M3 threaded rod (13) and an M3 nut (12) to seal the cell. The two parts of the flow cell were connected with the help of the Kapton tube (4), which was then sealed to the flow cell body at both ends using a heat shrink tube (15). The other end of the M3 rod from the working electrode was secured to the flow cell holder (11) with the help of another M3 nut. The assembled flow cell including the flow cell holder was fastened to the beamline sample stage using M6 bolts (10).

3. Experimental procedure

3.1. Beamline setup

Neutron experiments were carried out at the Imaging and Material Science & Engineering (IMAT) beamline [34]. IMAT is a cold neutron instrument located on target station 2 at the ISIS Facility [38]. Neutron wavelengths ranging between 0.5 and 15 Å with maximum flux around 3 Å are provided by a liquid hydrogen moderator on target station 2. IMAT has the capability to perform various imaging and diffraction analyses such as neutron radiography, neutron tomography, Bragg edge (diffraction) imaging, and allows investigations of strain, texture, and phase compositions via neutron diffraction. Neutrons travel from the H-moderator source along a flight path of 56 m, through a chopper system to selected energies between 1.6 and 81.8 meV (1–7 Å wavelength range) and through a pin-hole collimator to define L/D. Neutrons

impinge on the sample mounted on a 360-degree rotating stage along with linear translation in x, y, z axes [34]. For this study, transmitted neutrons were converted into photons by a 65×65 mm^2 ZnS/LiF scintillator screen with a thickness of 60 μm mounted inside a camera box including also a mirror with an inclination of 45°, focusing lens and a Charge-Coupled Device camera (CCD) (ANDOR IKON-L, 2048×2048 pixels, 30 μm pixel size) where the final image was formed on a 26 mm sized sensor (Figure S1). For imaging, the neutron beam size (i.e., 40 mm and 60 mm) was set to encompass the whole flow cell including the X65 sample. For diffraction, the neutron beam was reduced to just encompass the X65 sample.

X-ray experiments were performed at the Dual Imaging and Diffraction (DIAD) beamline located at Diamond Light Source facility (UK) [35]. DIAD comprises of a sequence of optical arrangements where two independent beams run parallel towards the sample allowing either imaging or diffraction in rapid succession (Figure S2). Flat X-ray mirrors M1, M3 are used to reflect a portion of the beam for imaging, while the M2 and M4 mirrors are used to collimate the remaining half of the reflected beams for diffraction (Figure S2). A double crystal monochromator system (DCM1 and DCM2) allows the selection of energies required for imaging and diffraction data acquisition. This is followed by a beam selector with a rotational mechanism for switching between imaging and diffraction. The focusing mirror optics are then used to pinpoint the beam onto the sample, having rotational and linear translation stage for imaging and diffraction. In this study, a wavelength of 0.4 Å was selected for an imaging beam size of 1.7 mm x 1.7 mm, with an effective pixel size of 0.54 μm. For diffraction, a beam footprint onto the sample of 5 μm x 15 μm was used [35].

3.2. Materials used

In this study, among the three electrodes of the flow cell, the material of interest chosen as the working electrode was API 5 L X65 steel, commonly used in industrial infrastructure. X65 is a low carbon steel composed by ~99 % Fe with trace amounts of carbon, silicon, manganese, phosphorus, sulphur, vanadium, niobium and titanium, as per the petroleum and natural gas industrial standards used in transportation of gas, water, and oil (Table S1). In X65 steel nomenclature, the number 65 indicates minimum yield strength produced by the pipeline (in Kilopound per Square Inch, KSI). The diameter of the X65 grade sample used in the experiments was limited to a maximum of 3 mm to overcome imaging limitations. The counter and reference material used for the flow cell experiments were platinum and Hastelloy wire of 1 mm diameter each. To test the flow cell, corrosion experiments were performed using a copper wire of 0.5 mm diameter coiled on the top of the steel sample. The inclusion of this wire creates a difference in electrochemical potential [39] that accelerates the corrosion reaction needed to test imaging and diffraction at synchrotron facilities.

The X65 steel sample was placed at the bottom part of the flow cell (Fig. 2b). An O-ring of 6 mm outer diameter and 4 mm inner diameter was placed underneath the sample to seal and prevent any leakage. The sample was then tightly attached to the flow cell with the help of a threaded rod, a washer, and a hexagonal nut for airtight fitting. Polytetrafluoroethylene (PTFE) tubing of 1/16" outer diameter and 0.031" inner diameter was used for inlet and outlet tubing connections from the ports of the cell that were secured with the help of acrylate glue for sealing. Tubing of 6 mm outer diameter and 4 mm inner diameter was used to connect the pump to the flow cell with the help of threaded adapters (1/16" OD x 1/4" - 28 UNF Male and 0.050" Bore, Male Luer Lock Female 1/4–28 flat bottom). The counter and reference electrode were inserted into the ports of the flow cell with the help of a tapered rubber stopper, having 3 mm and 7 mm diameter at each end with a hole of 1 mm diameter to insert the electrodes. The top and bottom cell parts were attached to the Kapton tube with a heat shrink tube.

3.3. Sample preparation

A X65 steel sample of 3 mm top hat diameter was progressively polished using silicon carbide papers with grit size of 240, 400, and 600 using a Struers LaboPol 60 polishing machine. During polishing, the sample was rinsed and maintained in acetone. After the final polishing, it was rapidly rinsed with DI water and dried using heated air. The sample was then stored in vacuum inside a sealed bag prior the test to avoid contact with air or water.

3.4. Corrosion experiment setup

The schematic setup of the corrosion experiments conducted at IMAT and DIAD beamlines is shown in Fig. 3. It is worth noting that the composition and structure of the sample is not affected by the neutron and X-ray radiations used in this work. The experimental setup included a sealed glass reactor with electrolyte (3.5 % NaCl) solution fitted with a glass condenser containing ethylene glycol as a coolant. A small outlet at the top of the reactor allowed to maintain a positive pressure in the system. The electrolyte solution was heated with a hot plate (IKA C-MAG HS7 digital) fitted with a probe to control temperature. The pH was monitored throughout the reaction using a pH probe and a pH meter (Mettler Toledo). The solution was circulated from the reactor through the cell and back to the reactor using a peristaltic pump (Ismatec ISM901). The electrolyte flowed in a closed loop within the sealed reactor and flow cell to ensure the composition of the solution remained unaltered through the experiment. To avoid entangling of the tubing during 360° tomography scans, the cell was rotated from −180° to 180° to obtain a complete 360° scan. The three electrodes of the flow cell were connected to the potentiostat (Gamry 1010E) to allow electrochemistry data collection. The experiment started by pumping the solution into the flow cell and by applying the required voltage/current to initiate the corrosion process. A drip trap was attached to the flow cell holder in case of an unexpected leakage (Figure S3).

3.5. Experimental methodology

An oxidation corrosion experiment was performed at IMAT to test the custom-flow cell as part of method development for steel corrosion studies. Details of the setup used are shown in figure S4. An uncorroded X65 steel sample was prepared as described in 3.3 with a copper wire coiled on the top surface. 700 ml of 0.1 M HCl solution were added to the reactor, followed by addition of sodium chloride to make it to 3.5 % concentration and heated to 60° C.

Before the corrosion was initiated, reference tomography data of the uncorroded sample were collected for ~5 h using a pin-hole of 40 mm, 201 projections with 1.8° step angle, and 80 s of exposure time per projection, (Figs. 4a and S4). After collection of reference data, the electrolyte solution along with 10 ml of H_2O_2 (30 wt% in H_2O) was pumped into the flow cell at 0.15 m/s flow rate. Galvanostatic corrosion was initiated by providing a constant current supply of 1 mA/cm^2 for 4 h. During the corrosion process, rapid tomography data were collected for 20 min after the 1st and 3rd hour using a pin-hole of 60 mm, 101 projections with a 3.582° step angle, and 10 s exposure time per radiogram. Since neutrons are strongly attenuated by water, the electrolyte solution was flushed out immediately before data collection to ensure tomography data could be collected. At the end of the corrosion cycle (i.e., after a further 4 h), tomography data were collected for 7 h
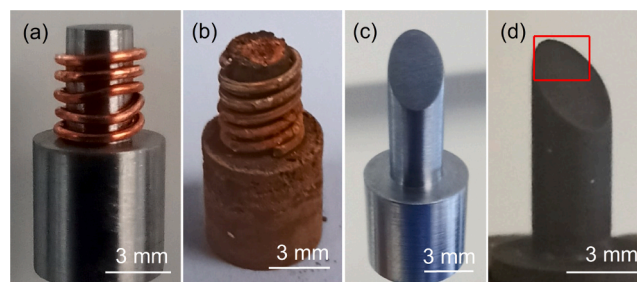

Fig. 4. (a) Uncorroded X65 steel sample coiled with copper wire before the start of the corrosion experiment, (b) Corroded steel sample after 4 h of oxidation corrosion, (c) Uncorroded sample before the in-situ experiment, (d) CO_2 corroded sample from the flow cell with siderite film on the surface. Red box indicates the region of interest of 1.4 mm× 1.2 mm selected for imaging and diffraction.

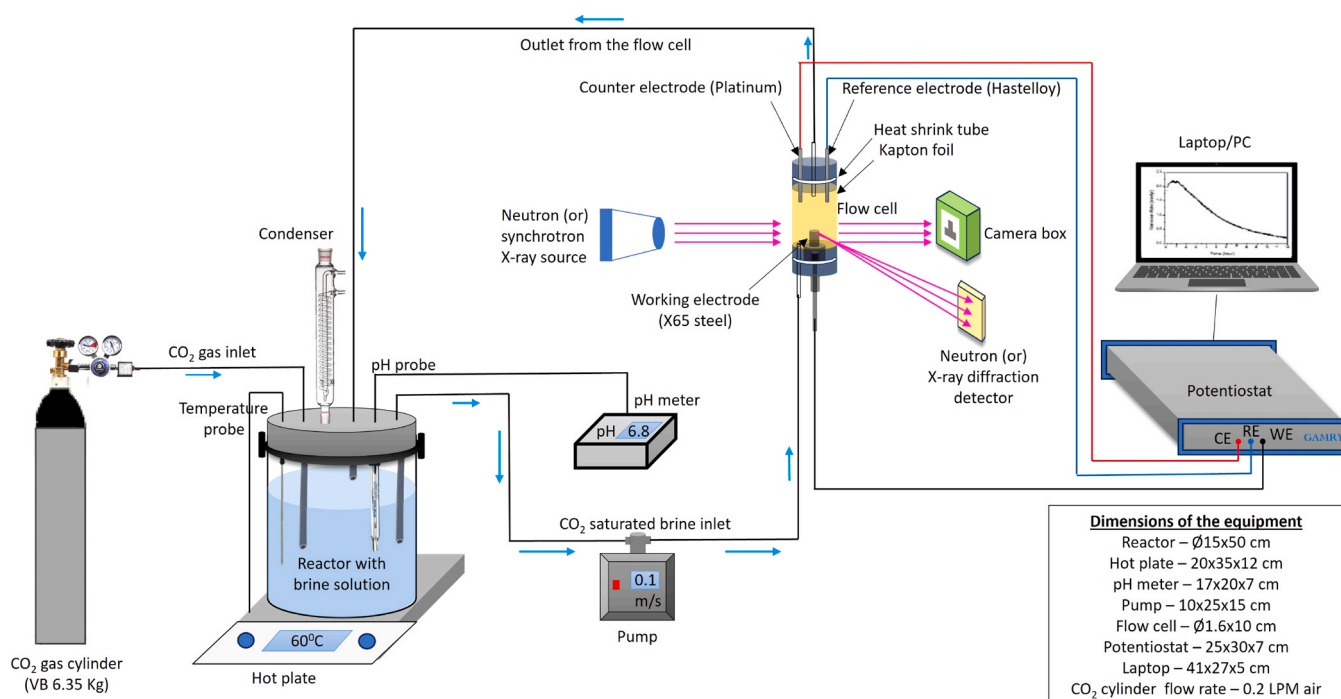**Fig. 3.** Schematic setup of the corrosion experiment at IMAT and DIAD beamlines.

using a pin-hole of 40 mm, 201 projections and a 1.8° step angle, and 120 s of exposure time. The sample at the end of the corrosion experiment is shown in Fig. 4b. The cell was removed, and 5 'open beam' and 10 dark images (neutron shutter closed) were collected to normalize the tomography data. The data were reconstructed using Mantid imaging tool [40] with 50 iterations of the CIL (PDHG-TV) algorithm. The reconstructed data were processed with Kip Tool v2.7 [41] for smoothing and denoising using the Inverse Scale Space (ISS) filter and TV-1 regularization with the following parameters: lambda= 0.1, tau= 0.125, alpha= 1.25 and 15 iterations for background removal. The processed data was further analysed in Avizo 3D v2023.1.1 [42] using watershed segmentation approach to distinguish steel from corrosion products. Masking was carried out for two phases, namely steel with copper and oxidised products, during the thresholding process. The threshold levels of these phases were selected from the histogram for all slices of a specified volume and the segmentation process was carried out using the watershed tool [43] available in the segmentation editor.

In addition, ex-situ neutron diffraction data were collected from an uncorroded and corroded (oxidized) sample coiled with a copper wire inside the flow cell. The pin-hole collimator was removed, and a wider wavelength range (0.5–6.5 Å) was used, to maximize neutron flux for diffraction. The neutron beam size and region of analysis was limited to 8 mm high and 13 mm wide by using neutron absorbing boron-carbide slits of 3 mm thickness in front of the flow cell. Additional boron-carbide sheets were used to block unwanted neutron scattering reaching the diffraction detectors. The uncorroded sample was scanned for one hour, while the corroded sample was scanned for 10 h to overcome the limited number of diffraction detectors. The diffraction patterns obtained were normalized with data collected from a solid 8 mm diameter vanadium rod, which provides a pattern free of Bragg peaks, and by collecting open beam data, i.e. blank scan without any sample in the beam.

A corrosion experiment in CO_2 environment was performed at DIAD, in which the electrolyte solution was saturated with CO_2 (Figure S5). As X-rays have low transmission in steel, a sample with 45° top surface inclination was used (Fig. 4c). In-situ tomography analysis was performed during the corrosion reaction as X-rays are hardly attenuated by water. A 3.5 % NaCl solution was prepared and saturated with CO_2 gas for a period of 6 h at 60° C, while maintaining the pH of the mixture to 6.8 by the addition of $NaHCO_3$. The CO_2 saturated brine solution was then pumped into the flow cell at a flow rate of 0.15 m/s. The galvanostatic corrosion experiment was initiated by applying a constant current of 2 mA/cm^2 for 4 h along with continuous CO_2 bubbling throughout the experiment. The sample at the beginning of the experiment and after the corrosion reaction is shown in Fig. 4. After placing the sample in the flow cell, it was aligned to a field of view of 1.4 mm× 1.2 mm (see red box indicating region of interest, ROI in Fig. 4d). X-ray tomography data and diffraction patterns were acquired from the uncorroded sample as the reference. For tomography, a total of 4000 projections were collected for ~7 min, with an exposure time of 0.1 s per projection. For diffraction, 20 points along each side of the rectangular ROI were analysed with an exposure time of 4 s each and a total diffraction collection time of ~27 min. Tomography data were filtered using KipTool v2.7 [41] for edge-preserving smoothing, using the same parameters listed above for the neutron data analysis. A Lanczos filter was applied to the data in Avizo [42] with a sigma value of 2 for smoothing and kernel size of 5 along x, y and z axes to improve signal to noise before segmentation process. Three phases were chosen for thresholding namely steel, siderite and empty space (porosity). Threshold levels of the phases were determined from the histogram, followed by segmentation using the watershed tool [43] available in the segmentation editor. 'Generate surface' and 'surface view' tools were used for viewing the post processed results in 3D, while the label analysis tool was used to list the volume data of each phase present for both IMAT and DIAD datasets. Here, we present imaging and diffraction data from uncorroded and corroded samples after 180 min of the corrosion process. Additionally, the imaging and diffraction results from the two

beamlines were supported with Scanning Electron Microscopy (SEM), Energy Dispersive X-ray Spectroscopy (EDS) and X-ray Diffraction (XRD) observations.

4. Results and discussion

4.1. Neutron tomography and diffraction using NX-DRT flow cell at IMAT

#### 4.1.1. Neutron tomography results

NX-DRT cell was initially tested using neutron imaging at IMAT, followed by X-ray imaging at DIAD to evaluate its capabilities and contribute for the method development for corrosion studies. Fig. 5a shows a radiogram of the flow cell, displaying the three electrodes, at the beginning of the experiment. For the corrosion experiment, the field of view was limited to the size of the yellow box to reduce unwanted neutron scattering from both the cell and any residual brine solution in the cell. Fig. 5b depicts a radiogram with the field of view for data acquisition. Using an open-beam normalized radiogram, it was established that the reduction in transmission by the Kapton window was less than 5 % within the pixel range of the steel sample (Fig. 5c). Fig. 6 shows a sequence of radiograms collected at the beginning of the experiment (time 0) and after the 1st, 3rd, and 4th hour. The radiograms illustrate the reduction in the sample height of ~90 μm after 4 h of oxidation corrosion. The top part of the sample was selected for further 3D analysis, as the lower part of the flow cell contained residual brine solution (Fig. 6).

Reconstructed tomography data were visualized for a small volume (Ø3 mm×2 mm height) using Avizo [42] as shown in Fig. 7. The 3D image of the uncorroded sample can be observed having a flat top surface along with a copper wire coiled on the top (Fig. 7a). Imaging artifacts were identified on the top surface of the steel sample, resulting in an uneven surface in a depth range corresponding to ~1 pixel equivalent to ~30 μm. However, artifacts were left at this stage, and no further smoothening was performed to avoid loss of information from corrosion products. After the 1st hour of corrosion, material from the top of the steel sample (above and adjacent to the copper wire) has disappeared, and the corrosion products are filling the gaps between the steel and the copper wire (Fig. 7b). This is expected to occur due to the electrochemical potential difference between steel and copper [39]. As the corrosion proceeds towards the 3rd and 4th hour, a drastic sample size reduction is observed with a significant material loss leaving a large pit on the surface (Figs. 7c and 7d).

Further segmentation analysis in Avizo [42] using a watershed algorithm allowed the differentiation of steel/copper from corrosion layers (Figs. 7e to 7h). The corrosion layers are shown in red whilst the material shown in green is associated with both steel and copper as the two metals are difficult to separate with neutron attenuation imaging. Figs. 7i to 7l show 3D cross-sectional images from data segmentation to illustrate the corrosion progress after 0, 1, 3, and 4 h. Figs. 7m to 7p show the corresponding 3D images after segmenting out the corrosion products, to better observe the damage caused to the steel material. The data show degradation of steel over time and growth of the corrosion layer. Material degradation started with the build-up of corrosion around the cooper wire (Figs. 7f and 7j) and continued with accumulation of corrosion layers on the steel cylinder surface (Figs. 7g and 7k), resulting substantial degradation of steel after 4 h of corrosion (Figs. 7h and 7l). During the process, significant damage was quantified, with ~30 % of material loss from cropped steel region (Fig. 7m), starting after one hour at the copper steel interface (owing to galvanic coupling, Fig. 7n) and eventually affecting all surfaces along with deeper pit penetration of pits (Fig. 7p). These data allowed to quantify the extend of internal degradation within the material at specific x, y, or z positions, with the error of segmented volumes estimated to be ~0.1 mm^3. The IMAT setup was limited to a spatial resolution of 60 μm and therefore, any oxide materials formed below this threshold could not be separated
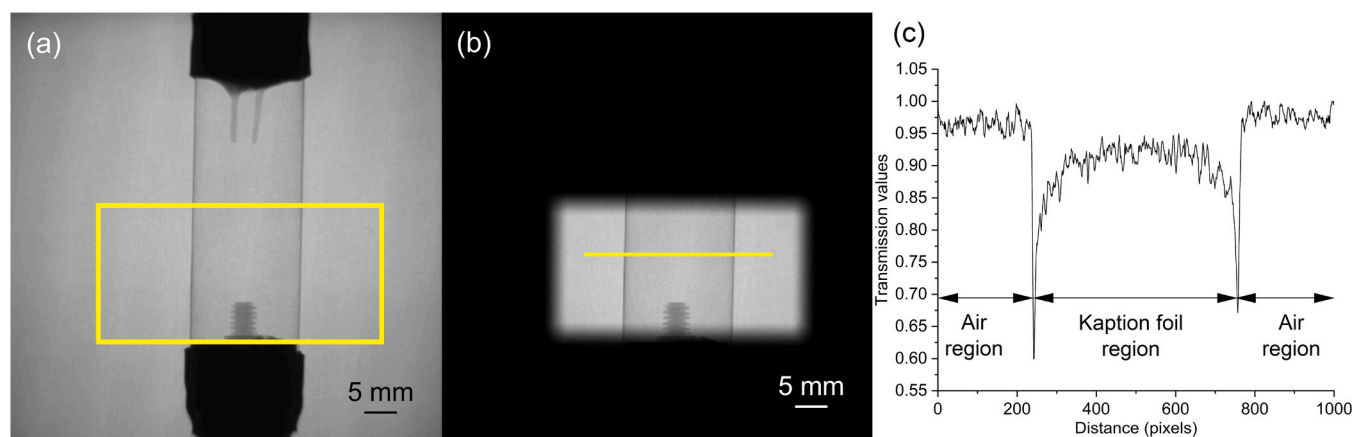
Fig. 5. Neutron radiography of (a) full flow cell, (b) flow cell with restricted field of view, (c) transmission profile plot across the flow cell following the yellow line indicated in (b).
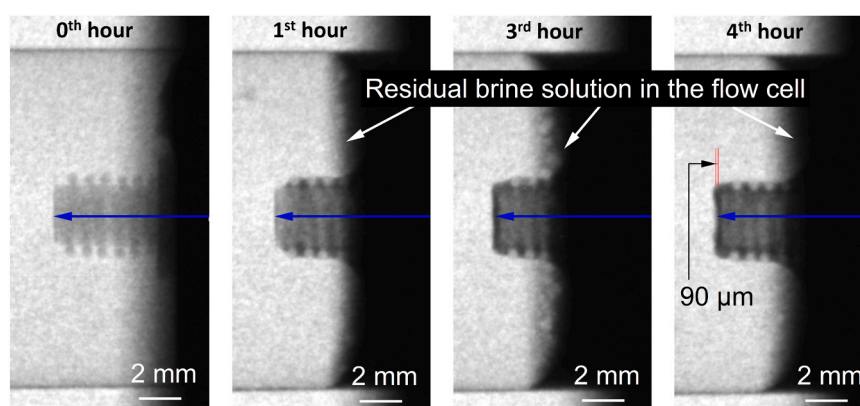
Fig. 6. Oxidation corrosion progress illustrated by neutron radiograms after 0, 1, 3, and 4 h.

from the underlying material.

Volumes of components in the uncorroded and corroded sample were calculated after segmentation as presented in Table 2 for the abovementioned region of interest. The progression of steel degradation versus the formation of the corrosion layer can be followed in Figure S6, showing the gradual decrease of steel material as corrosion products form over time with a loss of 4.6 mm^3 in 4 h. The rate of volume loss is 15.9 % at the end of the first hour, drops to 8.7 % at the end of third, before rising again to 9.5 % after four hours (Figure S6). A relatively fast corrosion process, in the order of hours, was designed in this work to demonstrate the capabilities of the imaging-diffraction methods developed here to include the designed flow cell, material selection, experimental and beamline setup and data processing. Our results indicate that the method was successfully developed to follow and quantify the degradation of materials (e.g., steel corrosion under different study conditions). Comparing with SEM analysis, pits smaller than 30 μm are evident in SEM images (Figure S7) but not visible in the neutron data due to the current spatial resolution limit. There is ongoing effort to improve spatial resolution at IMAT offer a promise of detecting smaller features in future [44]. For higher resolution, and in order to resolve fine corrosion features such as early pit formation or sub-surface film porosity, the experiment can be performed at high-flux neutron imaging beamlines with resolutions below 10 μm [45]. On the other hand, strong attenuation of neutron by water molecules limits the feasibility of in-situ experiments for neutron imaging. To enable data collection, the corrosion process needs to be paused and the electrolyte back-flushed making X-rays analysis with high resolution of ~3 μm the preferred choice to resolve fine features and for actual in-situ measurements.

### 4.1.2. Neutron diffraction results

Neutron diffraction was tested for first time at IMAT using our developed method and the new flow cell. Figure S8 depicts neutron diffraction patterns obtained from the uncorroded and corroded sample using time-of-flight diffraction detectors on IMAT. It is worth to mention that for this study two out of fourteen scintillation diffraction detector modules were used as the other twelve were at the installation stage at the time we conducted the experiments. Neutron diffraction data were collected for 10 h to compensate for limited detection coverage. The diffraction pattern of the corroded sample revealed the presence of iron and copper; however, Bragg peaks of corrosion products were below the detection limit. This is likely due to the small particle size of the corrosion products confirmed by SEM (Figure S7) that requires longer times of collection of diffraction data to be identifiable. Identification of the corrosion phases requires a systematic study and depends on the purpose of the study, highlighting the need for the refinement of the method for any specific application. The diffraction patterns of the empty flow cell indicate minimal diffraction background generated by the flow cell (Figure S8). XRD and EDS analysis from this experiment revealed the presence of different phases composing the corrosion materials, including Fe and Fe_3C from steel, while hematite (Fe_2O_3), magnetite (Fe_3O_4) and goethite FeO(OH) were identified as corrosion products (Figure S9- S11).

4.2. X-rays synchrotron tomography and diffraction at DIAD

4.2.1. X-rays synchrotron tomography results

Imaging results of the uncorroded and corroded samples are
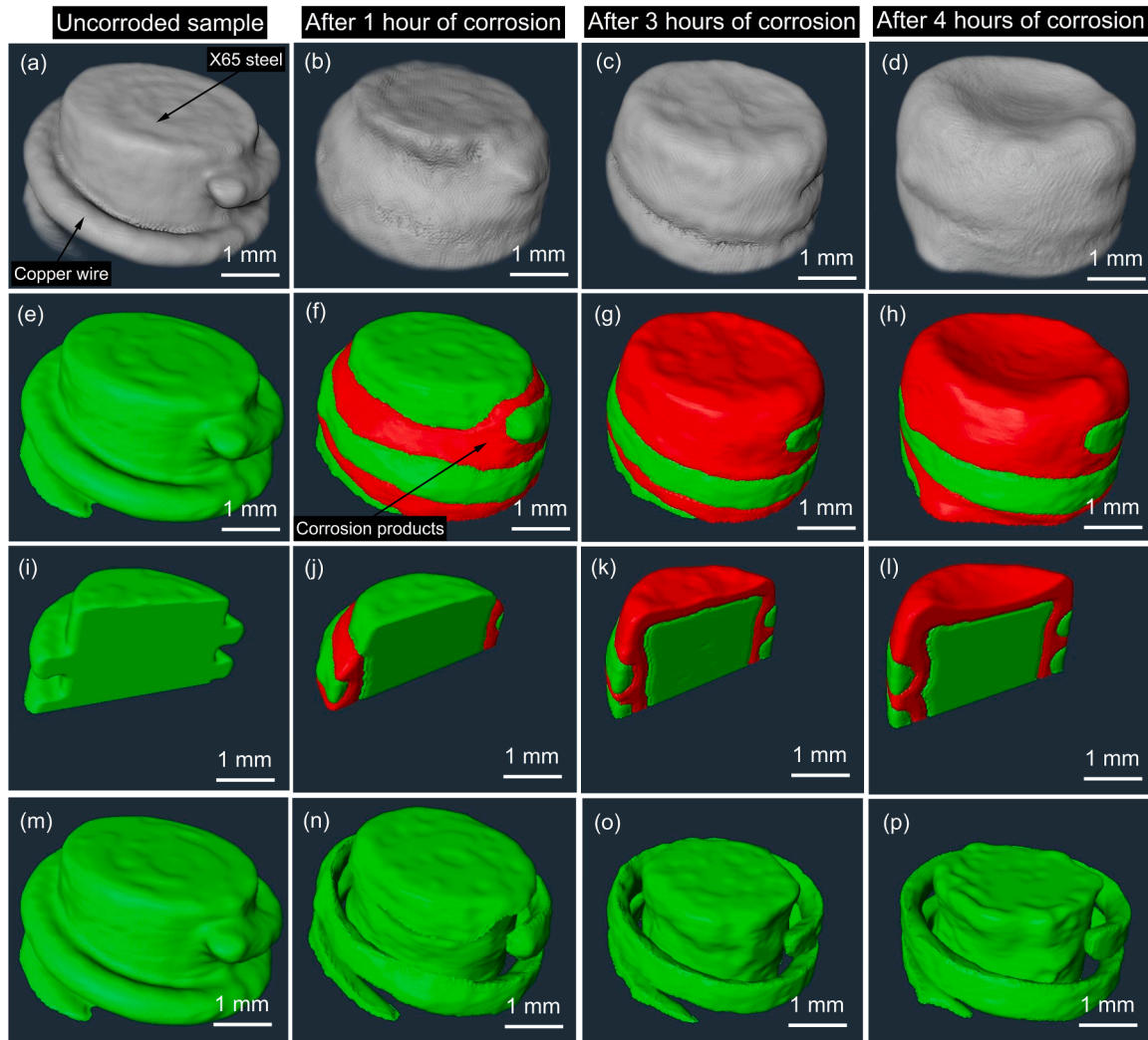
Fig. 7. Rendered and segmented volumes from neutron imaging. (a) 3D image of uncorroded steel sample with the coiled copper wire; (b), (c) and (d) 3D image of corroded steel sample after 1st, 3rd, and 4th hour; (e) 3D image of uncorroded steel sample after segmentation; (f), (g) and (h) 3D segmentation image of corroded steel sample after 1st, 3rd, and 4th hour. Green colour – steel and copper, red colour - corrosion products. (i) cross-sectional view of uncorroded steel sample; cross-sectional views of corroded steel sample after (j) 1 h, (k) 3 h, and (l) 4 h of exposure to electrolyte solution illustrating the material damage occurring with time. (m), (n), (o) and (p) 3D representation of steel/copper after having segmented out corrosion products after 1st, 3rd and 4th hour. Data were collected at IMAT with a imaging spatial resolution of about 60 μm.

Table 2

Quantitative analysis of sample component volumes (Ø3 mm×2 mm height) post segmentation from 3D imaging at IMAT.

	Uncorroded sample	Corroded sample (1 h)	Corroded sample (3 h)	Corroded sample (4 h)
Volume of steel + copper (mm^3)	15.1	12.7	11.6	10.5
Volume of corroded products (mm^3)	-	4.3	7.8	8.4
Percentage reduction in volume of steel (%)	-	16	23	31

presented in Fig. 8. A small sub-volume (~100 ×100 x 100 μm^3) of the dataset was selected to reduce demands on data processing times. The selected volume is shown in Fig. 8a. 3D views of reconstructed datasets from both uncorroded and corroded samples are shown in Figs. 8b and 8c, respectively. These images correspond to a region composed of 200

slices out of 2159 slices from the top surface along the z-axis. Similar to the neutron tomography data, the image of the uncorroded sample shows a rough surface that indicates the presence of artifacts despite the sample having been polished before the experiment (Fig. 8b). Such artifacts can be filtered using available smoothening tools; however, applying filters to the corroded sample may affect the information extracted from steel degradation and corrosion films. The image of the corroded sample, under a 3-hour CO_2 corrosion process, shows clear signs of material degradation (marked in Fig. 8c) with a corrosion film of ~10 μm in thickness and the presence of pits (indicated in Fig. 8c).

The 3D reconstructed data were analysed in Avizo [42] as presented in Fig. 8. The 3D volume was segmented using a watershed algorithm analogous to the data processing applied to the neutron data (Figs. 8d and 8e). The images show steel in green, siderite in red and porosity in yellow. Segmented volumes clearly reveal large interconnecting pores and cavities at the interface between the film and steel (Figs. 8c and 8e). This has been also observed in SEM analysis data as shown in Figure S12. The film shows signs of fracture visible as open pores of 1–20 μm in size (Figs. 8c, 8e and S12). X-ray tomography clearly indicates the extent of degradation (with a volume reduction of 12.9 ×10^{-6} mm^3 after 3 h of corrosion), pits formed on the steel surface at multiple points on the
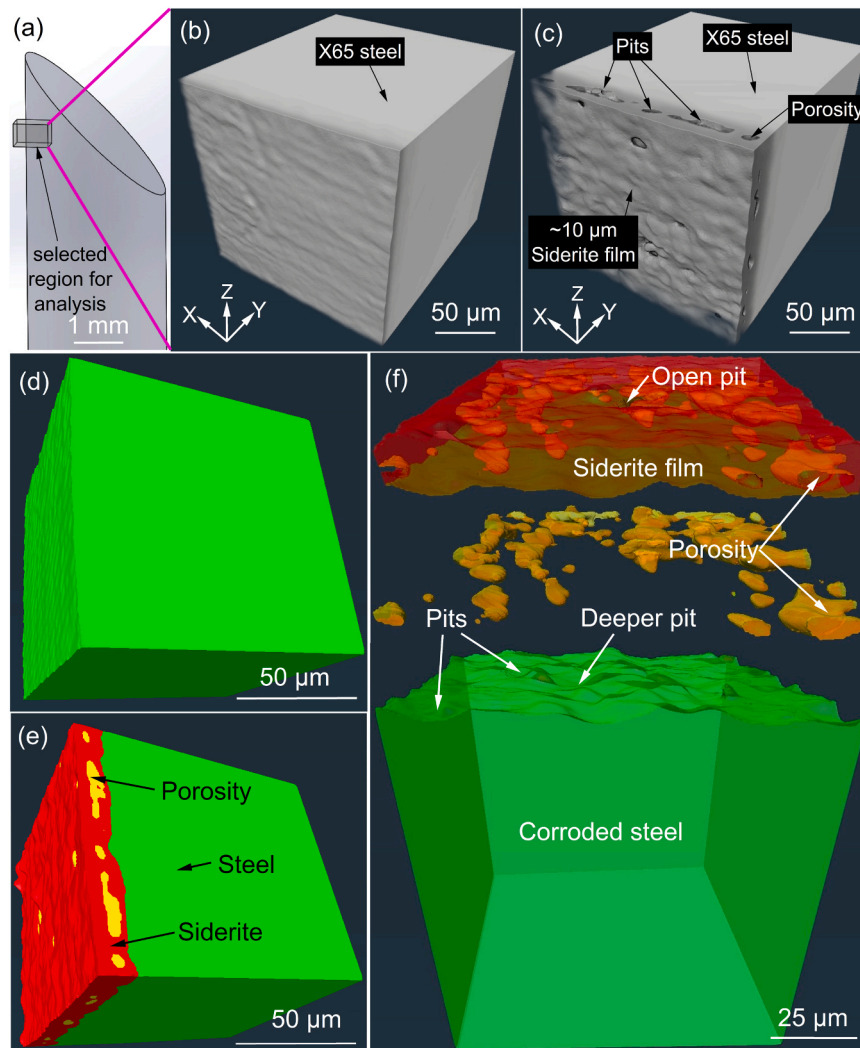
Fig. 8. (a) 45^0 inclined X65 steel sample schematic representation; cube inside steel sample: selected region for analysis of 700–900 reconstruction slices out of 2159 slices; (b) and (c) Volume-rendered synchrotron X-ray tomography data of uncorroded sample, and corroded sample after 180 min; (d) and (e) 3D image of uncorroded and corroded steel sample after segmentation. The images show the separation of steel, siderite and pores (green colour – steel material, red colour – siderite, yellow colour – pores); (f) Exploded 3D view of corroded steel, siderite and porosity demonstrating siderite and porosity layer over steel substrate. Data were collected at DIAD, Diamond Light Source, UK with a spatial resolution of ~3 μm.

sample and the degradation to the steel surface after 3 h of corrosion (Figs. 8c and 8e). A full 3D view of the corrosion film, porosity and pits can be observed in Fig. 8f which reveals an open pit in the siderite film, exposing the steel substrate underneath accelerating corrosion. Volume quantification was performed on uncorroded and corroded samples, with results tabulated in Table 3. Approximately 1 % of reduction in volume of steel material was observed at the end of 3 h. Additionally, the volumes of siderite and pores are approximately 10 % and 1 %, respectively, relative to the volume from the sub-sample analysed.
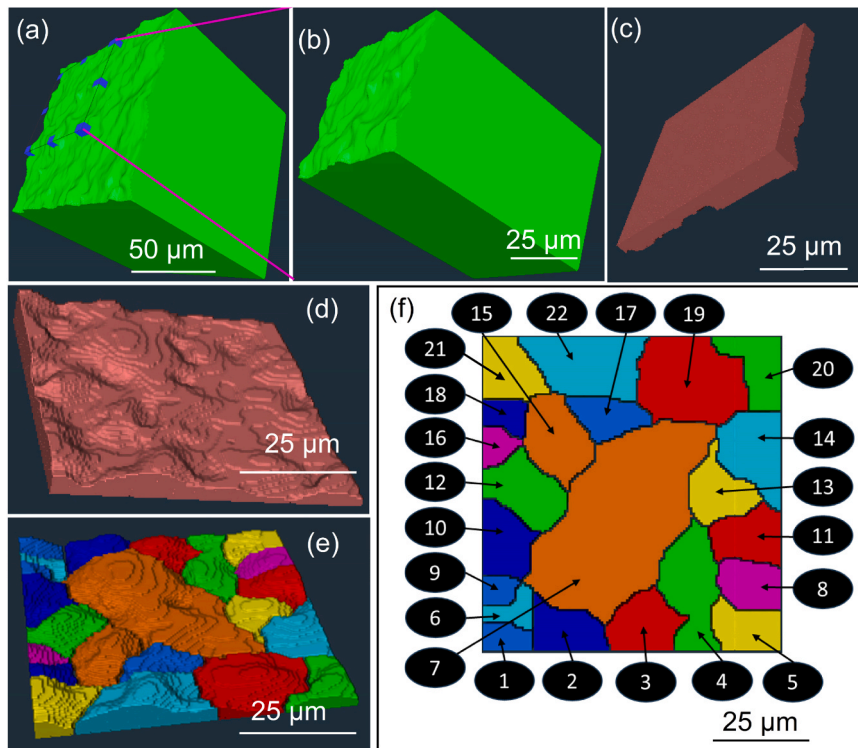
Therefore, relative to the volume of the siderite film, the pore volume amounts to about 10 %. The progression of film formation and porosity as well as the progression of steel degradation can be also quantified and will be presented in a forthcoming paper. Future analysis will provide deeper insight and will aid in elucidating the time-dependent corrosion mechanism.

To further analyse pitting on the corroded steel sample, a sub volume with a surface area of 65×65 μm^2 was extracted (Figs. 9a and 9b). The selected region of interest touched all the edges of the sample from where pits originated. An XOR logical operation was applied to this surface to extract the pit volume from steel (Fig. 9c). The "separate objects" tool distinguished two adjacent pits, followed by distance mapping to assess the pitting corrosion parameters. The morphology of the pits is illustrated in Fig. 9d. The label analysis of the data provided the colour mapping of the individual pits (Fig. 9e). The maximum and minimum depth of pits relative to the corroded surface was found to be 27.51 μm and 0.32 μm. The areas, volumes and height of all the pits (Fig. 9f) formed on the corroded steel surface are presented in Table 4. Some of these range of pit depths are represented in cross-section SEM image of the corroded sample as depicted in Figure S13.

Table 3
Quantitative analysis of corroded sample sub-volume (~100 ×100 x 100 μm^3) post segmentation from 3D imaging at DIAD. The error of segmented volumes is ~0.01 × 10^{-6} mm^3.

	Uncorroded sample	Corroded sample (3 h)
Volume of steel (mm^3)	1289.8 × 10^{-6}	1276.9 × 10^{-6}
Volume of Siderite (mm^3)	-	116.3 × 10^{-6}
Porosity volume (mm^3)	-	14.8 × 10^{-6}
Percentage reduction in volume of steel (%)	-	~1

Fig. 9. (a) 3D image of degraded steel after segmenting out siderite and porosity for pitting corrosion analysis; (b) degraded steel region cropped from blue box, $65 \times 65\ \mu m^2$ in (a); (c) pitting corrosion layer extracted after performing XOR logical operation; (d) pitting corrosion morphology visualization; (e) colour mapping of each pit from (d); (f) pit numbering from 1 to 22 (top view of (e)).

Table 4
Pitting corrosion volume, area and height quantification of corroded sample of selected region, $65 \times 65\ \mu m^2$.

Pit number	Volume (μm^3)	Area (μm^2)	Minimum height (μm)	Maximum height (μm)	Mean height (μm)
1	426	322	0.5	16.8	7.4
2	924	563	0.5	24.7	11.7
3	1011	584	0.7	23.3	11.4
4	1087	772	0.5	12.4	6.9
5	674	468	0.6	12.3	6.8
6	342	312	0.5	17.5	10.6
7	5426	2547	1.3	27.5	11.8
8	616	424	1.4	14	7.6
9	284	237	1.2	17	8.9
10	912	566	0.4	17.4	9.1
11	676	489	0.4	13.9	6.8
12	888	586	0.6	14.2	7.4
13	520	431	1.2	8.9	5.4
14	615	545	0.3	7.8	3.7
15	843	578	1.1	12.6	6.8
16	215	205	0.5	8.4	4.8
17	459	374	1	11.2	6.6
18	249	228	0.7	10.8	5.5
19	1080	865	0.5	8.2	4.1
20	402	416	0.4	5.9	2.7
21	663	478	0.6	12.1	5.7
22	1237	819	0.5	14.6	6.2

4.2.2. X-rays synchrotron diffraction results

In-situ synchrotron X-ray diffraction analysis was performed at DIAD along with 3D imaging analysis as described in 3.5. An area was selected from the front face of the sample composed of a 20-point grid for diffraction collection. X-ray diffraction data confirmed the presence of siderite, as expected, conforming with a corrosion film on the steel surface Figure S14, and with XRD, SEM and EDS data (Figures S12, S15 and S16).

5. Conclusion

This work presents an imaging and diffraction technology that revolutionizes in-situ corrosion studies, enabling unprecedented insights into mechanisms of corrosion formation and material degradation. In this work, we have designed, evaluated, and tested a three-electrode NX-DRT flow cell for 3D imaging and diffraction. This innovative flow cell, coupled with a bespoke experimental setup, has demonstrated exceptional performance, providing precise quantitative data on corrosion progression rates and material degradation through neutron and X-ray radiation imaging within a few microns of spatial resolution, offering great penetration depth. Remarkable efficacy of the method is shown with detailed insights into corrosion formation, corrosion thickness, porosity, pitting, and electrochemical data. This dual approach successfully yields comprehensive structural data marking a significant leap forward in the field of corrosion analysis.

The NX-DRT flow cell has been developed to enable sequential in-situ imaging and diffraction analysis and can be used with a variety of materials. The results from in-situ diffraction, radiography, and tomography confirm that this innovative flow cell is an indispensable tool for advanced corrosion studies, utilizing both neutrons and synchrotron X-rays. The NX-DRT flow cell facilitates tomographic and temporal (4D) imaging, allowing researchers to monitor the degradation of samples in three-dimensional space and at multiple time points throughout the corrosion process. This capability marks a significant advancement in understanding and analysing material degradation, providing critical insights into corrosion mechanisms. Diffraction data further support the identification of corrosion products formed on the steel surface over time. This in-situ flow cell enables a time-dependent analysis of film growth and simultaneous damage to the underlying material, facilitated by advanced tools capable of phase-specific segmentation for detailed spatial investigation. Pitting corrosion can now be quantified from 3D image analysis, offering a comprehensive spatial surface analysis of pitting in terms of volume, area, maximum height, and minimum height

at the micron scale. Topographical mapping of pit distribution across the surface enhances visualization of corrosion-induced surface degradation. Overall, our work demonstrates the unprecedented capability of the in-situ flow-cell to conduct degradation studies and elucidate mechanisms in ways never before possible.

The experiment conditions used in this work were far from real-world conditions, as compromises were made for the development of the in-situ combined imaging and diffraction method, and for efficient use of beamtime at large-scale X-ray and neutron facilities. However, more tailored experiments with specific conditions can be designed, especially as the new flow cell facilitates in-situ corrosion studies on low carbon steel and other materials, assessing inhibitor performance [46], studying the effect of flow rates [47–51] for different compositions of alloys and sample geometries. Future work will address the integration of the electrochemical data and image registration of the corroding surface to the newly developed flow cell method. Registration will be achieved using 'baseline' data on the blank sample before any corrosion has commenced, and/or by referencing via voxel distance measurements from a unique sample geometry aspect (for example, top of 45-degree slanted sample surface) or relative to fiducial features located on the corroding surface or inside the steal substrate.

CRediT authorship contribution statement

Adriana Matamoros-Veloza: Writing – review & editing, Supervision, Project administration, Methodology, Investigation, Funding acquisition, Data curation, Conceptualization. **Nikil Kapur:** Writing – review & editing, Supervision, Project administration, Methodology, Conceptualization. **Vicky Ullas Mirashi:** Writing – review & editing, Writing – original draft, Methodology, Investigation, Formal analysis, Data curation, Conceptualization. **Winfried Kockelmann:** Writing – review & editing, Supervision, Project administration, Methodology, Investigation, Data curation, Conceptualization.

Declaration of Competing Interest

The authors declare the following financial interests/personal relationships which may be considered as potential competing interests: Adriana Matamoros-Veloza reports financial support was provided by ISIS Pulsed Neutron and Muon Source. Adriana Matamoros-Veloza reports financial support was provided by Diamond Light Source Ltd. Adriana Matamoros-Veloza reports statistical analysis was provided by Image analysis from the National Facility in XCT at University of Warwick. If there are other authors, they declare that they have no known competing financial interests or personal relationships that could have appeared to influence the work reported in this paper.

Appendix A. Supporting information

Supplementary data associated with this article can be found in the online version at doi:10.1016/j.corsci.2025.113417.

Data availability

Data underlying the results presented in this paper are not publicly available at this time but may be obtained from the authors upon reasonable request.

References

[1] Davis, J.R. 2000, Corrosion: Understanding the Basics, Knovel Library. ASM International, 563, ISBN: 0871706415, 9780871706416.

[2] P.R. Roberge. Handbook of Corrosion Engineering, second ed., McGraw-Hill Education, LLC, New York, 2012. ISBN: 9780071750370.

[3] K. Trethewey, J. Chamberlain, Corrosion for Science and Engineering, second ed., 1, Pearson Education, 1995, p. 466. ISBN: 0-582-23869-2.

[4] G. Koch, Cost of corrosion. Trends in Oil and Gas Corrosion Research and Technologies: Production and Transmission, Woodhead Publishing Series in Energy, 2017, pp. 3–30, https://doi.org/10.1016/B978-0-08-101105-8.00001-2.

[5] Koch, G., Varney, J., Thompson, N., Moghissi, O., Gould, M., & Payer, J., International measures of prevention, application, and economics of corrosion technologies study, in: Proceedings of the NACE International, 216, Mar. 2016, [Online]. ⟨http://impact.nace.org/documents/Nace-International-Report.pdf⟩.

[6] NACE International, The Real Cost of Corrosion, Rust Bullet, Mar. 2017 [Online]. ⟨https://www.rustbullet.com/cost-of-corrosion/⟩.

[7] Overholt, M., The Importance of Oil and Gas In Today's Economy, Aug. 2016 [Online]. https://www.tigergeneral.com/the-importance-of-oil-and-gas-in-today-s-economy/⟩.

[8] R. Singh. Applied Welding Engineering - Processes, Codes, and Standards, third ed., Elsevier, 2020 https://doi.org/10.1016/B978-0-12-821348-3.00001-X. ©.

[9] Parkins, R.N., A review of stress corrosion cracking of high pressure gas pipelines, in: Proceedings of the CORROSION 2000, Orlando, Florida, NACE-00363, 2000, ⟨https://onepetro.org/NACECORR/proceedings-abstract/CORR00/All-CORR00/NACE-00363/112101⟩.

[10] R.N. Tuttle, Corrosion in oil and gas production, J. Pet. Technol. 39 (07) (1987) 756–762, https://doi.org/10.2118/17004-PA.

[11] M. Askari, M. Aliofkhazraei, S. Afroukhteh, A comprehensive review on internal corrosion and cracking of oil and gas pipelines, J. Nat. Gas. Sci. Eng. 71 (2019), https://doi.org/10.1016/j.jngse.2019.102971.

[12] A.H. Al-Moubaraki, I.B. Obot, Corrosion challenges in petroleum refinery operations: sources, mechanisms, mitigation, and future outlook, J. Saudi Chem. Soc. 25 (12) (2021), https://doi.org/10.1016/j.jscs.2021.101370.

[13] M.A. Baker, The application of surface imaging techniques to the study of pitting corrosion initiation in stainless steels, Surf. Interface Anal. 20 (6) (1993) 535–543, https://doi.org/10.1002/sia.740200609.

[14] E.O. Fanijo, J.G. Thomas, Y. Zhu, W. Cai, A.S. Brand, Surface characterization techniques: a systematic review of their principles, applications, and perspectives in corrosion studies, J. Electrochem. Soc. 169 (11) (2022) 111502. ⟨https://iopscience.iop.org/article/10.1149/1945-7111/ac9b9b⟩.

[15] L. Niu, Y. Yin, W. Guo, M. Lu, R. Qin, S. Chen, Application of scanning electrochemical microscope in the study of corrosion of metals, J. Mater. Sci. 44 (17) (2009) 4511–4521, https://doi.org/10.1007/s10853-009-3654-x.

[16] D. Dwivedi, K. Lepkova, T. Becker, Emerging surface characterization techniques for carbon steel corrosion: a critical brief review, Proc. R. Soc. A 473 (2017), https://doi.org/10.1098/rspa.2016.0852.

[17] K. Yasakau, Application of AFM-Based techniques in studies of corrosion and corrosion inhibition of metallic alloys, Corros. Mater. Degrad. 1 (2020) 345–372, https://doi.org/10.3390/cmd1030017.

[18] R.M. Souto, S. Lamaka, S. González, Uses of scanning electrochemical microscopy in corrosion research, Microscopy Science Technology Applications Education 3 (2010). ⟨https://www.researchgate.net/publication/255738960⟩.

[19] L. Luo, L. Zou, D.K. Schreiber, et al., In-situ transmission electron microscopy study of surface oxidation for Ni-10Cr and Ni-20Cr alloys, Scr. Mater. 114 (2016) 129–132, https://doi.org/10.1016/j.scriptamat.2015.11.031.

[20] "Metropolitan Engineering, Consulting & Forensics (MECF) - Root Causes And Contributing Factors Of Gas And Liquid Pipeline Failures, [Online]. ⟨https://sites. google.com/site/metropolitanforensics/root-causes-and-contributing-factors-of-ga s-and-liquid-pipeline-failures⟩.

[21] S.S. Al-Jaroudi, A. Ul-Hamid, M.A. Al-Moumen, Premature failure of tubing used in sweet extra arab light grade crude oil production well, Eng. Fail. Anal. 47 (part A) (2015) 178–198, https://doi.org/10.1016/j.engfailanal.2014.10.006.

[22] S. Robuschi, A. Tengattini, J. Dijkstra, I. Fernandez, K. Lundgren, A closer look at corrosion of steel reinforcement bars in concrete using 3D neutron and X-ray computed tomography, Cem. Concr. Res. 144 (2021), https://doi.org/10.1016/j. cemconres.2021.106439.

[23] I.S. Anderson, R.L. McGreevy, H.Z. Bilheux, Neutron imaging and applications, ©, Springer Science+Business Media, LLC, 2009, https://doi.org/10.1007/978-0-387-78693-3.

[24] J. Postletitwaite, R.A. Brierley, Electrochemical flow cell for elevated temperature/ pressure aqueous corrosion studies, Corros. Sci. 10 (12) (1970) 885–890, https:// doi.org/10.1016/S0010-938X(70)80108-1.

[25] Nor, A.M., The Effect of Turbulent Flow on Corrosion of Mild Steel in High Partial CO2 Environments, Doctor of Philosophy, Ohio University, Athens, 2013. [Online]. Available: ⟨https://www.ohio.edu/engineering/sites/ohio.edu.engineering/files/ sites/engineering/The-Effect-of-Turbulent-Flow-on-Corrosion-of-Mild-Steel-in-High-Partial-CO2-Environments_A-Mohammed-Nor_2013_PhD.pdf⟩.

[26] C. Madore, D. Landolt, The rotating cylinder hull cell: design and application, Plat. Surf. Finish. 80 (11) (1993) 73–78. ⟨https://www.pfonline.com/cdn/cms /1501_printable_version.pdf⟩.

[27] K.E. Duncan, B.M. Perez-Ibarra, G. Jenneman, J.B. Harris, R. Webb, K. Sublette, The effect of corrosion inhibitors on microbial communities associated with corrosion in a model flow cell system, Appl. Microbiol. Biotechnol. 98 (2) (2014) 907–918, https://doi.org/10.1007/s00253-013-4906-x.

[28] R. Barker, B. Pickles, N. Kapur, T. Hughes, E. Barmatov, A. Neville, Flow cell apparatus for quantitative evaluation of carbon steel corrosion during transitions in fluid composition: application to transition from inhibited hydrochloric acid to sodium chloride brine, Corros. Sci. 138 (2018) 116–129, https://doi.org/10.1016/ j.corsci.2018.04.012.

[29] D. Burkle, R.D. Motte, W. Taleb, et al., Development of an electrochemically integrated SR-GIXRD flow cell to study FeCO3 formation kinetics, Rev. Sci. Instrum. 87 (10) (2016), https://doi.org/10.1063/1.4965971.

[30] J.A. Wharton, R.J.K. Wood, Influence of flow conditions on the corrosion of AISI 304L stainless steel, Wear 256 (5) (2004) 525–536, https://doi.org/10.1016/ S0043-1648(03)00562-3.

[31] T. Binninger, E. Fabbri, A. Patru, M. Garganourakis, J. Han, D.F. Abbott, Electrochemical Flow-Cell setup for in situ X-ray investigations, J. Electrochem. Soc. 163 (10) (2016) H906–H912. ⟨https://iopscience.iop.org/article/10. 1149/2.0201610jes⟩.

[32] A. Kreta, M. Gaberšček, I. Muševič, Time-resolved in situ electrochemical atomic force microscopy imaging of the corrosion dynamics of AA2024-T3 using a new design of cell, J. Mater. Res. 36 (1) (2021) 79–93, https://doi.org/10.1557/ s43578-020-00077-2.

[33] G.T. Van de Kerkhof, J.M. Walker, S. Agrawal, et al., An in situ liquid environment for synchrotron hard X-ray nanoprobe microscopy, Mater. High. Temp. 40 (4) (2023) 371–375, https://doi.org/10.1080/09603409.2023.2213579.

[34] T. Minniti, K. Watanabe, G. Burca, D.E. Pooley, W. Kockelmann, Characterization of the new neutron imaging and materials science facility IMAT, Nucl. Instrum.

Methods Phys. Res. A 888 (2018) 184–195, https://doi.org/10.1016/j. nima.2018.01.037.

[35] C. Reinhard, M. Drakopoulos, S.I. Ahmed, et al., Beamline K11 DIAD: a new instrument for dual imaging and diffraction at diamond light source, J. Synchrotron Radiat. 28 (2021) 1985–1995, https://doi.org/10.1107/ S1600577521009875.

[36] C. Örnek, F. Léonard, S.A. McDonald, et al., Time-dependent in situ measurement of atmospheric corrosion rates of duplex stainless steel wires, Npj Mater. Degrad. 2 (1) (2018), https://doi.org/10.1038/s41529-018-0030-9.

[37] SOLIDWORKS® Premium 2022 SP5.0," © 1995 - 2022 Dassault Systemes. [Online]. ⟨https://www.solidworks.com/⟩.

[38] IMAT (Imaging and Materials Science & Engineering)- Neutron imaging and diffraction instrument at ISIS Neutron and Muon Source. [Online].⟨https://www.is is.stfc.ac.uk/Pages/Imat.aspx⟩.

[39] H.P. Hack, Evaluation galvanic corrosion, corrosion: fundamentals, in: Testing, and Protection, ASM Handbook, 13A, ASM International, 2003, pp. 562–567. ISBN: 0-87170-705-5.

[40] Tygier, S., Akello-Egwel, D., Allen, J., et al., Tomographic reconstruction with Mantid Imaging, in: Journal of Physics: Conference Series, Institute of Physics, 2023, ⟨https://iopscience.iop.org/article/10.1088/1742-6596/2605/1/012017⟩.

[41] C. Carminati, M. Strobl, A. Kaestner, KipTool, a general purpose processing tool for neutron imaging data, SoftwareX 10 (2019), https://doi.org/10.1016/j. softx.2019.100279.

[42] Thermo Fisher ScientificTM, Avizo 3D 2023.1.1. [Online]. ⟨http://www.ther mofisher.com/amira-avizo⟩.

[43] S. Beucher, F. Meyer, The morphological approach to segmentation: the watershed transformation, first Edition, Math. Morphol. Image Process. (1993) 433–481, https://doi.org/10.1201/9781482277234-12.

[44] V.U. Mirashi, W. Kockelmann, N. Kapur, et al., Exploring spatial resolution enhancements on IMAT for steel corrosion studies, Nucl. Instrum. Methods Phys. Res. A 1073 (2025), https://doi.org/10.1016/j.nima.2025.170284.

[45] A. Tengattini, N. Lenoir, E. Andò, et al., NeXT-Grenoble, the neutron and X-ray tomograph in grenoble, Nucl. Instrum. Methods Phys. Res. A 968 (2020), https:// doi.org/10.1016/j.nima.2020.163939.

[46] A. Shamsa, R. Barker, Y. Hua, et al., Impact of corrosion products on performance of imidazoline corrosion inhibitor on X65 carbon steel in CO2 environments, Corros. Sci. 185 (2021), https://doi.org/10.1016/j.corsci.2021.109423.

[47] X. Chen, X. Yang, M. Zeng, H. Wang, Influence of CO2 partial pressure and flow rate on the corrosion behavior of N80 steel in 3.5% NaCl, Int. J. Electrochem. Sci. 18 (8) (2023), https://doi.org/10.1016/J.IJOES.2023.100218.

[48] K. Li, Y. Zeng, J.L. Luo, Influence of H2S on the general corrosion and sulfide stress cracking of pipelines steels for supercritical CO2 transportation, Corros. Sci. 190 (2021), https://doi.org/10.1016/j.corsci.2021.109639.

[49] A. Ravikumar, P. Rostron, N. Vahdati, O. Shiryayev, Parametric study of the corrosion of API-5L-X65 QT steel using potentiostat based measurements in a flow loop, Appl. Sci. 11 (1) (2021) 1–17, https://doi.org/10.3390/app11010444.

[50] L. Zeng, G. Chen, H. Chen, Comparative study on flow-accelerated corrosion and Erosion–Corrosion at a 90° carbon steel bend, Materials 13 (7) (2020), https://doi. org/10.3390/MA13071780.

[51] Kvarekval, J., Gulbrandsen, E., High Temperature and High Flow Velocity Tests for CO2 Corrosion Inhibitors, in: Proceedings of the CORROSION 2001. CORROSION 2001, Houston, TX, AMPP, 1-20, 2001, https://doi.org/10.5006/C2001-01025.